Express Polymer Letters Vol.16, No.11 (2022) 1177–1192
Available online at www.expresspolymlett.com
https://doi.org/10.3144/expresspolymlett.2022.86

Research article

Visible-light enhanced photocatalytic performance by lowering the bandgap of reusable TiO_2/chitin and ZnO/chitin nanocomposites for trimethoprim degradation

Jonás José Perez Bravo[1,2,3,5], *María Emilia Villanueva*[1,3,4], *Gabriel Ibrahin Tovar*[1,3], *Nora Judit François*[2,4], *Guillermo Javier Copello*[1,3*]

[1]Universidad de Buenos Aires. Facultad de Farmacia y Bioquímica. Departamento de Ciencias Químicas. Buenos Aires, Argentina
[2]Grupo de Aplicaciones de Materiales Biocompatibles, Departamento de Química, Facultad de Ingeniería, Universidad de Buenos Aires (UBA), C1063ACV, CABA, Argentina
[3]CONICET – Universidad de Buenos Aires. Instituto de Química y Metabolismo del Fármaco (IQUIMEFA). Buenos Aires, Argentina
[4]Universidad Nacional de Luján (UNLu) Departamento de Ciencias Básicas, Ruta 5 y 7 Luján, Buenos Aires, Argentina
[5]CONICET-Universidad de Buenos Aires. Instituto de Tecnología de Polímeros y Nanotecnología (ITPN-UBA-CONICET), Buenos Aires, Argentina

Received 27 January 2022; accepted in revised form 4 July 2022

Abstract. For a nanocomposite, the interaction among nanoparticles (NPs) and the polymeric matrix acting as support has a determinant role in the performance of the material in its intended application. Two UV-sensitive NPs (TiO_2 and ZnO) were chosen in order to study the effect of their interaction with chitin in the photocatalytic degradation of trimethoprim, which is an emerging pollutant. Chitin-NPs composites were characterized by structural, thermal, optical, and photoelectrochemical techniques. NPs immobilization into the chitin matrix showed to affect both NPs in the same manner by influencing their photocurrent generation and decreasing the bandgap, which allowed taking advantage of the Visible-light spectrum. Trimethoprim degradation rates under simulated sunlight and chitin chemical stability upon reusability were evaluated. Both composites can be used over a wide range of pH, but the alkaline medium produced a decrease in the chitin:ZnO degradation efficiency. The chemical structure of chitin was not affected by the photocatalysis reaction, even after several cycles. As it was observed for the nude NPs, the chitin:TiO_2 composite trimethoprim degradation efficiency was higher than the chitin:ZnO nanocomposite. Chitin matrix allowed an easy recovery of the NPs from the treatment medium and recycling of the material without loss of photocatalytic efficiency.

Keywords: *nanocomposites, chitin, photocatalytic degradation, trimethoprim, emerging pollutant*

1. Introduction

Population growth and industrialization have caused environmental contamination by different pollutants. Some contaminants may be mobile and persistent in air, soil, and water, even at low concentrations. Their behavior, fate, and ecotoxicological effects have not been often well understood. The main reason is that many of these compounds, also called emerging pollutants (EPs), have been classified as such for a very short time. EPs are chemicals without regulatory status, and their effects on human health and the environment are unknown [1, 2]. Pharmaceutical products, such as antibiotics, are of particular concern because their massive use can

*Corresponding author, e-mail: gcopello@ffyb.uba.ar
© BME-PT

produce antibiotic-resistant bacteria posing a severe threat to ecosystems and human health [3, 4]. Several kinds of antibiotics have been detected in underground water and river systems, among which trimethoprim, ciprofloxacin, enrofloxacin, norfloxacin, ofloxacin, and roxithromycin have been reported [5]. Effiuents from wastewater treatment plants are regarded as the primary source of these pollutants [6, 7]. Different conventional treatment methods such as adsorption, ultrafiltration, coagulation, and heterogeneous photocatalysis, among others, have been used to remove EPs from waters. Heterogeneous photocatalysis is an advanced oxidation technology (AOT) and a promising strategy to remove EPs. Heterogeneous photocatalysis has several advantages, such as high mineralization yields and plausible reuse of many catalysts, which lowers the process costs. Moreover, the new photocatalysts aim to be effective under solar light irradiation as a sustainable energy source [8].

Several semiconductor photocatalysts, including TiO_2 and ZnO nanoparticles (NPs), have attracted attention due to their potential applications in the degradation of aqueous EPs [9]. They are environmentally benign, biocompatible, abundantly available, and low cost. The main drawback of using nanosize particles comes from their difficult recovery from suspensions after the photocatalytic process. This hampers their regeneration and reuse when large water volumes are required to be treated. Providing NPs with support brings an important impact on their stability and recyclability. Nanostructured composite polymers have been considered an interesting alternative to enhance their recoverability, allowing regeneration, reuse, and minimizing their elution into the treated water [10, 11].

In the last years, the use of natural polymers obtained from renewable resources has raised the interest of society. Their use complies with the principles of the circular economy due to their renewable origin, biodegradability, and low costs [12]. Chitin is considered an environmentally friendly and low-cost material because it is a biodegradable, non-toxic, and biocompatible polymer normally obtained from crustacean waste [13, 14]. Chitin is less expensive and more stable (chemically) when it is compared to chitosan and its derivatives [13]. The poor solubility of chitin limits its application, and probably due to it, the literature shows few approaches yet dedicated to chitin composites [15]. Chitin nanostructured composites have been developed thanks to the manipulation techniques that have overcome the polymer's low solubility [13, 16–19]. These researchers reported the formation of chemically stable materials without toxic chemical cross-linking agents. From another perspective, other works used epichlorohydrin as a chemical cross-linker agent to improve the mechanical properties of hydrogels [20, 21].

In recent years, few but promising studies have used chitin as a support matrix for photocatalytic particles. Interesting performances have been reported focused on ammonium removal using UV irradiation [22], or dye degradation using chemical grafting on chitin in order to obtain a functional and reusable matrix under sunlight [11, 23–25]. These works raise the need to understand the effect of the NPs interaction with chitin and the effect of the photocatalytic event upon chitin chemical structure. Also, it has not been reported the obtaining of photocatalytic nanomaterial without previous chitin chemical modification (such as chitin deacetylation or for metal-organic framework production) or without toxic chemical cross-linking agents (such as epichlorohydrin or glutaraldehyde for the obtaining of reinforced materials). Thus, this work aimed to study the photocatalytic behavior of ZnO NPs and TiO_2 NPs in the degradation of EPs when immobilized in a chitin matrix. In this experimental design, the use of a non-cross-linked and non-modified material based on chitin and the influence of the loaded NPs photoactivity on the matrix structure during irradiation was able to be studied. Trimethoprim (TMP) degradation as an EP model was studied using simulated sunlight. The photoelectrochemical behavior and bandgap determination for the nanocomposites were studied in order to understand the effect of chitin on the NPs photocatalytic behavior. The chemical stability of chitin was studied among several photocatalytic degradation cycles. Also, physicochemical characterization of composites and the influence of composites' composition, medium pH, the influence and stability of the support, and the degradation kinetics on heterogeneous catalysis were discussed.

2. Materials and methods

2.1. Materials

Chitin from shrimp shells was obtained from Sigma-Aldrich, USA, the chitin degree of acetylation was 94%. Methanol HPLC grade was purchased from Sintorgan, Argentina. Ethanol of 99.5% purity and calcium chloride dihydrate were purchased from

Cicarelli, Argentina. Evonik Degussa Argentina SA donated the TiO_2 nanoparticles of AEROXIDE TiO_2 P-25 procured from Evonik, Germany. Trimethoprim was acquired from Saporiti, Argentina. Potassium dihydrogen phosphate, Potassium hydrogen phosphate, and Sodium hydroxide were acquired from Anedra, Argentina. Chemicals were used without further purification and the reagent grade was analytical.

2.2. Preparation of zinc oxide nanoplates

For ZnO NPs preparation, the method reported by Villanueva *et al*. [26] was employed. Zinc sulfate was mixed with urea until a homogeneous solution was obtained. The concentrations of urea and Zn^{2+} were adjusted to 3.3 and 2.4 mM in the solutions, respectively. Then a solution of 3 M NaOH was added drop-wise until a suspension was obtained. Following the observations regarding particle growth from the work of [27], water washing steps were performed before the composites synthesis, and the last washing step was performed in the methanol/calcium solution to be used in the preparation of the chitin hydrogel in order to reduce carbonates residuals and stabilize the particle.

2.3. Preparation of chitin hydrogel and chitin nanostructured composites

To prepare the reference chitin xerogel, 42.5 g of calcium chloride dihydrate were mixed in 50 ml of methanol and refluxed at 80 °C to near-dissolution. Then, 1 g of chitin powder was added to the calcium/methanol solution and refluxed at 90 °C for 2 h under constant stirring. Different mass ratios of chitin and TiO_2 NPs or ZnO NPs were mixed by agitation to obtain materials with a different percent of chitin:TiO_2 NPs (Chi:TiO_2-1, Chi:TiO_2-5 and Chi:TiO_2-10) and chitin: ZnO NPs (Chi:ZnO-1, Chi:ZnO-5 and Chi:ZnO-10). For example, 1 g of chitin, 42.5 g of calcium chloride dihydrate, and 50 ml of methanol suspension were mixed with 111 mg of TiO_2 to obtain a hybrid material with 10 wt%/wt of TiO_2 (Chi:TiO_2-10).

The chitin xerogel and chitin nanocomposites mixtures (chitin:TiO_2 NPs and chitin:ZnO NPs) were spun into a glass beaker with cold ethanol until they gelled. Finally, the gels were subjected to several distilled water incubations to wash out all the methanol, ethanol, and $CaCl_2$ residues. All prepared materials were oven-dried at 50 °C, milled, and sieved between 250 and 500 μm for all the experiments.

2.4. Characterization

2.4.1. Scanning electron microscopy (SEM) and energy dispersive spectroscopy (EDS)

Samples were hydrated, then freeze-dried (lyophilization) and coated with a 20 nm gold layer before being analyzed using a Philips 505 SEM and EDS analyzer. The micrographs were taken at 200× magnification.

2.4.2. Fourier transforms infrared spectroscopy (FTIR)

Attenuated total reflection Fourier-transform infrared spectrum (ATR-FTIR) of samples was recorded using a Thermo Scientific Nicolet iS50 Advanced Spectrometer (USA) with diamond attenuated total reflectance. All spectra were recorded at ambient temperature at the resolution of 4 cm^{-1}, 32 scans, and operating in the range of 4000–400 cm^{-1}. The degree of *N*-acetylation (*DA)* of chitin was determined according to the method proposed by Brugnerotto *et al*. [28] using Equation (1):

$$\frac{A_{1320}}{A_{1420}} = 0,3822 + 0,3133 \cdot DA \tag{1}$$

2.4.3. X-ray diffraction (XRD)

XRD patterns were obtained using a Philips 3710 diffractometer with graphite-monochromated (Cu-Kα radiation, at 40 kV–40 mA); with 0.03° and 3 s steps in the 5–80° 2θ range. The chitin crystallinity index (*CrI*) was determined by applying the method reported by Segal *et al*. [29] for cellulose and reported elsewhere. Equation (2) was used to calculate the crystalline index:

$$CrI = \frac{I_{020} - I_{am}}{I_{020}} \cdot 100 \tag{2}$$

where I_{020} was the maximum intensity at ≈10° and I_{am} was the amorphous contribution (maximum intensity) obtained at ≈16° as the general baseline [30]. The particle size for TiO_2 (17.6) and ZnO (32.8) were calculated using the Scherrer equation. Since the ZnO particles were stabilized within the chitin matrix, their particle size was calculated from the nanocomposite XRD pattern [31].

2.4.4. Thermogravimetric analysis (TGA)

The thermal degradation processes of the samples were investigated using a Shimadzu TGA-50 Instrument (Japan). The measurements were carried out by

heating the sample from 25 to 800 °C under an inert atmosphere (N_2 flow rate of 30 ml·min^{-1}), with a heating rate β = 10 °C·min^{-1} using a similar sample weight (approximately 10 mg).

2.4.5. Differential scanning calorimetry (DSC)

DSC measurements were performed in a Shimadzu DSC-60-Plus instrument (Japan). The samples were hermetically sealed in aluminum pans, and tests were developed under a dynamic N_2 atmosphere (30 ml·min^{-1}) using a sample weight of approximately 10 mg and a heating rate 10 °C·min^{-1}. The DSC tracings were performed from 25 to 250 °C.

2.4.6. UV-Vis spectroscopy

The absorption spectra (UV–Vis diffuse reflectance measurements) were obtained by a Shimadzu UV-2401 PC in the wavelength range of 200–800 nm in order to evaluate the optical properties. Barium sulfate was employed as a reference material (100% reflectance measurement).

2.4.7. Photoelectrochemical behavior

The photocurrent was recorded using a three-electrode cell configuration, with two Pt electrodes and one counter electrode under a 0.5 V *vs*. Ag/AgCl using a Palm Sense 4 electrochemical workstation (Netherlands). Thirty-five seconds cycles of light exposure (Xe lamp) were used. The suspension consisted of 10 mg of sample, $Cu(OAc)_2 \cdot 2H_2O$ 2.2 mM, HNO_3 0.02 M, and 25 ml acetic acid [32].

2.4.8. Trimethoprim quantification

The quantification was performed using an high-performance liquid chromatography (HPLC) system consisting of a Hewlett Packard 1050 pump with a 20 µL injection loop, a Supelco column RP 18 150×0.4 mm stationary phase, and a Waters 484 UV detector set at 250 nm. The separation was performed at room temperature by isocratic elution of the analyte using a mobile phase containing acetonitrile-water (0.6:0.4 v/v) and a flow rate of 1 ml·min^{-1}.

2.4.9. Photocatalytic experiments

The photocatalytic activity for the trimethoprim decomposition by the NPs and prepared nanocomposite were evaluated under two Xenon lamps irradiation with a power of 40 W for each lamp. The irradiation intensity for all assays was 22 000 lux, with less than 5% variation. Aqueous solutions of trimethoprim (5 ml, 20 mg·l^{-1}) were placed in a vessel, and 0.050±0.002 g of the nanocomposite samples were added. For a 0.005±0.002 g of free NPs an initial TMP concentration of 50 mg·l^{-1} was used. Samples of aliquots were taken up, centrifuged, and reserved for quantification at certain time intervals. Composites with different TiO_2 NPs and ZnO NPs concentrations (1, 5, and 10%) were exposed to 7 h intervals at room temperature. The reusability was evaluated using 50 mg of sample in seven consecutive runs. After each photocatalytic reaction, the samples were recovered by sedimentation, washed (using distilled water), and dried (overnight at 50 °C). Then, they were reused in another degradation cycle under the same experimental conditions. A solution of trimethoprim without adding any composite photocatalyst was used as a control study under the same conditions. The degradation fraction of trimethoprim was calculated by the Equation (3):

$$Degradation\ fraction = \frac{C}{C_0} \tag{3}$$

where C_0 and C are the initial and final concentrations of trimethoprim at $t = 0$ or time t, respectively. It is important to note that, after the preparation of the solution and before irradiation, all suspensions were shaken at dark for 30 min to reach adsorption/ desorption equilibrium. The kinetics of photocatalytic degradation of organic dyes usually follows the Langmuir–Hinshelwood mechanism (Equation (4)) [33]:

$$-r = \frac{\mathrm{d}C}{\mathrm{d}t} = \frac{kKC}{1 - KC} \tag{4}$$

where r is the degradation rate of trimethoprim [mg·l·min^{-1}], C is the concentration of the trimethoprim [mg·l^{-1}], t is the degradation time, k is the reaction rate constant [mg·l·min^{-1}], and K is the adsorption constant of the trimethoprim (l·mg^{-1}). When C is small, the equation is simplified to give the pseudo-first-order kinetic model with a determined rate constant (k_1) (Equation(5)) [34]:

$$C = C_0 \mathrm{e}^{-\mathrm{k_1 t}} \tag{5}$$

Also, the pseudo-second-order kinetics was studied (Equation (6)):

$$C = \frac{C_0}{1 + C_0 k_2 t} \tag{6}$$

where k_2 is the rate constant for a pseudo-second-order kinetic degradation [35].

2.4.10. Statistical analysis

All experiments and their corresponding measurements were conducted in triplicate under identical conditions and statistically analyzed by one-way ANOVA and Tukey comparison post test if ANOVA $p < 0.05$.

3. Results and discussion

3.1. SEM and EDS analysis

Figure 1 shows the morphology of chitin xerogel and prepared nanocomposites. The surface of the analyzed samples exhibited an irregular and porous-like morphology. In comparison to the chitin xerogel, the surface of the nanocomposites showed a rougher morphology. This was due to NPs dispersion into the chitin matrix that altered the surface. EDS was used to analyze the Zn and Ti content on the nanocomposites. The Zn and Ti mapping images revealed the NPs successful incorporation into the polymeric matrix. For Chi:ZnO-10 composite it could be observed a good dispersion of NPs into the chitin matrix, while for Chi:TiO_2-10 it could be appreciated the presence of zones with higher NPs density, even at the same loading content.

3.2. FTIR analysis

FTIR studies were conducted to gain insight into the functional groups features of the composites obtained with different NPs and compositions. Figure 2 shows the FTIR spectra obtained for the chitin xerogel, TiO_2 NPs, ZnO NPs, and the prepared composites. Figure 2 curve a showed a typical spectrum of chitin xerogel and its characteristic bands [36]. The two bands located at 1669 and 1524 cm^{-1} corresponded to the vibrational stretching of C=O (amide I) and N–H deformation and C–N–H vibrational stretching (amide II), respectively [36]. In Figure 2 curve b the typical bands from TiO_2 NPs spectrum between 3300–3600 cm^{-1} (stretching vibrations) and at 1622 cm^{-1} (bending vibrations) could be observed [13, 37]. The FTIR spectrum for ZnO NPs is shown

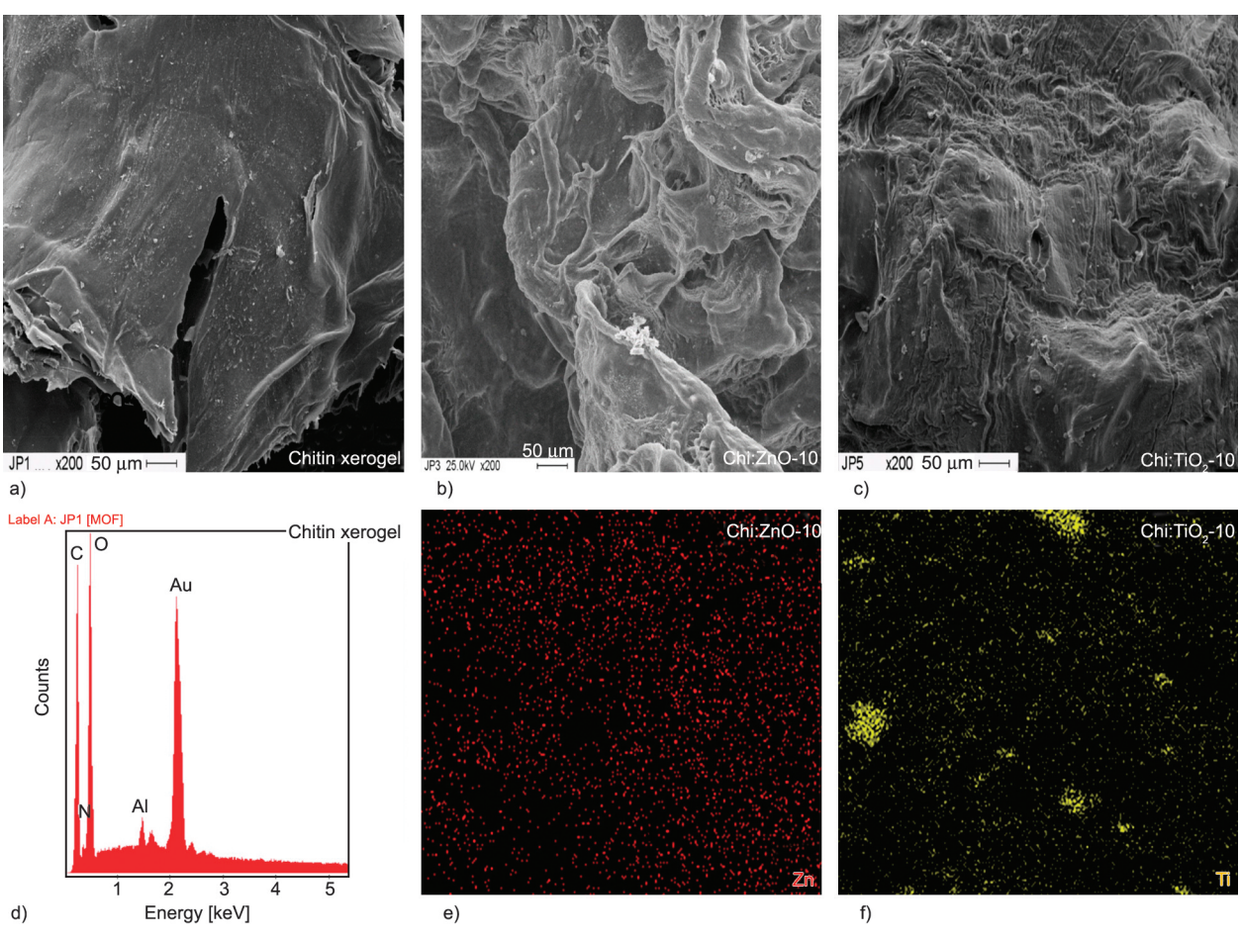

Figure 1. SEM images of a) chitin xerogel, b) Chi:ZnO-10 and c) Chi:TiO_2-10, d) EDS profile of chitin xerogel, e) Zn EDS mapping of Chi:ZnO-10 and f) Ti EDS mapping of Chi:TiO_2-10.

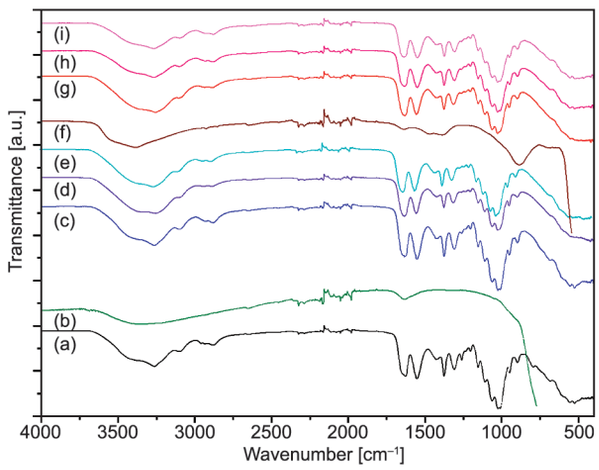

Figure 2. FTIR spectra of (a) chitin xerogel; (b) TiO_2 NPs; (c) Chi:TiO_2-10; (d) Chi:TiO_2-5; (e) Chi:TiO_2-1; (f) ZnO NPs; (g); Chi:ZnO-10 (h) Chi:ZnO-5; and (i) Chi:ZnO-1.

in Figure 2 curve f. The band present at 3280 cm^{-1} corresponded to the O–H stretching of the water molecules [26]. The broad peak around 3385 cm^{-1} was assigned to the O–H stretching mode of the hydroxyl group from associated water, and the band at 1634 cm^{-1} (bending) is due to asymmetrical stretching of the zinc carboxylate [38]. The bands at 957, 1029, and 1123 cm^{-1} correspond to the remains of the carbonate formed during the ZnO NPs formation [26]. These results suggest that ZnO NPs and $Zn_4CO_3(OH)_6 \cdot H_2O$ were present. The presence of the latter came from ZnO NPs synthesis. The Zn^{2+} reacted with the urea forming $Zn_4CO_3(OH)_6 \cdot H_2O$ and then was oxidized to obtain ZnO NPs. For every nanocomposites spectra, the bands corresponding to the NPs were not detected, probably due to its low content in the material. The composites spectra showed no new bands or shifts when compared to the chitin xerogel spectrum. This would mean that no chemical reaction occurred between the NPs and chitin, and probably weak interfacial interactions were predominant between the materials. Taking into account the moieties present in all components of the composites, these interactions could be H bonds between M–OH groups in the surface of the NPs and the –OH groups of the polysaccharide.

3.3. XRD analysis

X-ray diffraction results are shown in Figure 3. Chitin xerogel showed peaks at 9.58, 13.07, 19.65, and 26,59°, typical of α-chitin structure (Perez *et al.*, [4]). In Figure 3a the XRD patterns of the TiO_2 NPs presented peaks corresponding to anatase (25.30, 37.80, and 48.08°) and rutile crystalline phases (27.42°). Commercial TiO_2 (P-25) NPs were a mixture of anatase/rutile phase, and their composition was 85 and 15%, respectively [37]. At chitin:TiO_2 NPs composites patterns, three peaks were clearly visible (25.30, 37.80, and 48.08°), as shown in Figure 3a. This confirmed the TiO_2 NPs incorporation on composite samples. Comparing diffraction patterns of TiO_2 NPs and chitin:TiO_2 NPs composites,

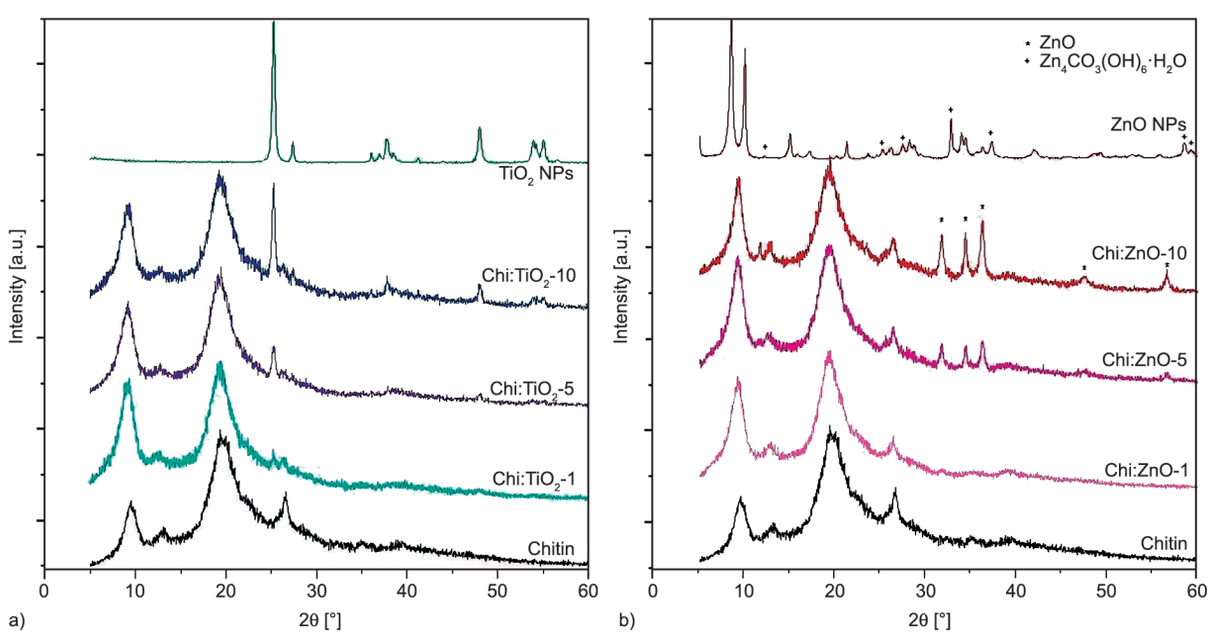

Figure 3. X-ray diffractograms of chitin xerogel, TiO2 NPs, ZnO NPs, and composites with different nanoparticles concentrations (1, 5 and 10%). a) TiO_2 NPs and Chi:TiO_2 composites, b) ZnO NPs and Chi:ZnO composites.

it is clear that the incorporation of NPs into the polymeric matrix does not affect the crystallinity of the nanoparticles. Figure 3b shows the XRD patterns of the ZnO NPs and prepared composites. ZnO NPs XRD pattern presented hexagonal wurtzite ZnO nanoplate peaks together with characteristic peaks of $Zn_4CO_3(OH)_6 \cdot H_2O$ [39, 40]. After the incorporation of ZnO NPs into chitin, the XRD pattern showed three wider bands typical of ZnO NPs, owing to the good dispersion and stabilization of nanoplates in the polymeric matrix. No carbonates peaks were observed on XRD patterns of chitin:ZnO NPs composites. As described in the works by Sun *et al*. [41] and Meulenkamp [27] the dispersion of ZnO NPs in the organic solvent (methanol/ $CaCl_2 \cdot H_2O$) solution would wash superficial carbonates and stabilize the particles in the composite matrix. This was confirmed by the presence of the ZnO crystallographic lattices 100 (31°), 002 (34°), and 101 (36°). Sun *et al*. [41] reported a similar phenomenon for purified ZnO nanoparticles in methanol solution. Moreover, in both hybrid systems (chitin:TiO_2 NPs and chitin:ZnO NPs) as the nanoparticles:chitin ratio increased, the characteristic nanoparticles peaks increased their intensity. Results confirmed the formation of biocomposites with different nanoparticles:chitin ratios. The fillers' interaction with chitin during the gelling step would decrease the crystalline zones of chitin and induce the decay in the crystallinity index, as shown in Table 1. The filler introduction reduced the degrees of freedom in the 3D composite conformation by inhibiting a close packing of the polymeric chains (amorphization), limiting or even preventing the formation of crystalline regions. These results suggested that the TiO_2 NPs and ZnO NPs induced a conformational change in the polymeric matrix.

Table 1. The crystallinity index (*CrI*) from XRD and thermal transition (T_p) from the DSC thermograms for chitin xerogel and composites.

Materials	*CrI* [%]	T_p [°C]
Chitin xerogel	51.1	111.5
Chi:TiO_2-1	38.6	110.2
Chi:TiO_2-5	37.5	84.7
Chi:TiO_2-10	35.6	81.9
Chi:ZnO-1	44.2	110.7
Chi:ZnO-5	43.9	88.1
Chi:ZnO-10	42.2	85.8

3.4. Thermogravimetric analysis (TGA)

Results of thermal stability analysis of chitin xerogel and the composites are shown in Figure 4. In the thermogram of chitin xerogel, chitin:TiO_2 NPs, and chitin:ZnO NPs composites, multiple-loss steps could be appreciated. The first step is observed in the range of 30–150 °C in all the samples, which was related to water evaporation. Xerogel chitin presented a higher amount of water loss compared to the composites. This would be due to the physical interaction between the fillers and the chitin polymer chain. The presence of the nanofillers would influence the chitin structure; this physical interaction probably would produce fewer free sites for the water to bound to the biopolymer. The second stage in thermograms analysis appeared between 250 and 350 °C for chitin xerogel and chitin:TiO_2 NPs composites and in a range of 250–400 °C for chitin:ZnO NPs composites. This weight loss could be attributed to the depolymerization of chitin [34, 42]. Notably, the nanofillers increased the thermal stability of composites, each at a different temperature range. The thermal stabilization effect was evident for chitin:ZnO composites in the second weight-loss stage but in the third for the chitin:TiO_2 composites. Thermograms showed that ZnO NPs improved the composite thermal stability. This phenomenon would be produced by the ZnO NPs geometry and/or nanoparticle size. These NPs probably acted as a mass transport barrier or thermal insulator to the volatile products generated during thermal decomposition by obstructing the escape of volatile compounds, producing a higher residual mass which in not proportional to the amount of incorporated ZnO NPs [43]. This behavior was

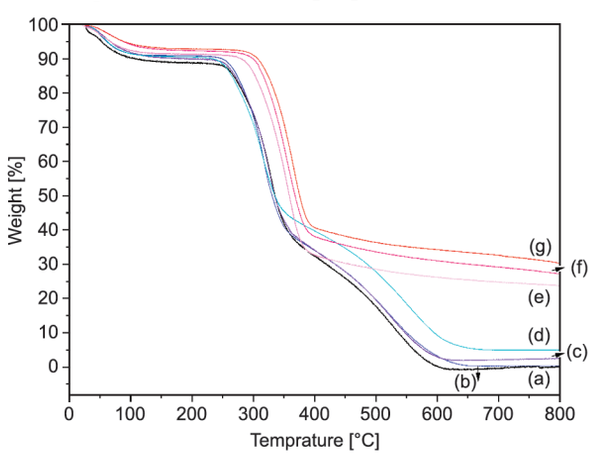

Figure 4. Thermograms of (a) chitin xerogel; (b) Chi:TiO_2-1; (c) Chi:TiO_2-5; (d) Chi:TiO_2-10; (e) Chi:ZnO-1; (f) Chi:ZnO-5; and (g) Chi:ZnO-10.

also observed for ZnO and gelatin nanocomposites [43]. Finally, the third stage for chitin xerogel and chitin:TiO_2 NPs composites from 350 to 600 °C was caused by the pyrolysis, vaporization, and elimination of the volatile products of chitin [42].

3.5. Differential scanning calorimetry (DSC)

Figure 5 shows the DSC curves of chitin xerogel and prepared composites. All the evaluated samples showed an endothermic peak associated with water evaporation. This thermal transition represents the required energy to vaporize water bound to the chitin xerogel and hybrid materials. Thermograms for chitin xerogel showed a broader endotherm peak around 111.5 °C, as shown in Table 1. Both nanofillers' incorporation into polymeric matrix induced molecular changes by shifting the position of the composites' endothermic peaks (T_p) to lower temperature values (Table 1). The shift was induced by the amorphization of composites due to the incorporation of the nanoparticles, as already discussed with the XRD and TGA results. This shift to lower temperatures is also in accordance with the discussed TGA results regarding the capability of the chitin to interact with water molecules when the nanoparticles are present.

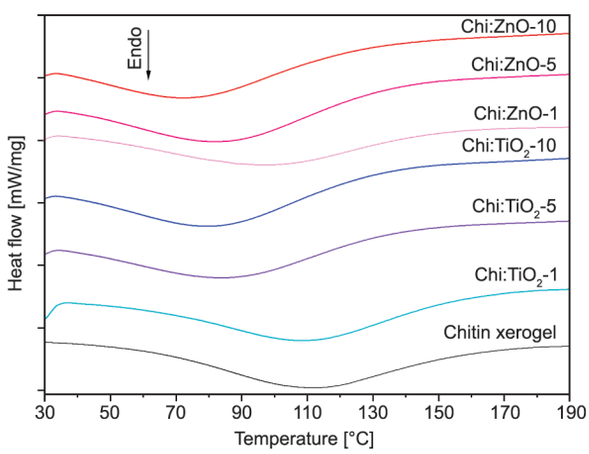

Figure 5. DSC curve of chitin xerogel, TiO_2 NPs, ZnO NPs, and composites with different nanoparticles concentrations (1, 5 and 10%).

3.6. Optical properties

The optical properties of chitin xerogel, NPs, and prepared composites were studied by diffuse reflectance spectroscopy (DRS), as shown in Figure 6a. The chitin xerogel spectrum presented a characteristic absorption band between 204 and 238 nm associated with the π-bond of the carbonyl functional group (C=O) [44]. It can be noticed that NPs and nanostructured composites presented light absorption capacity mostly in the UV region (λ < 400 nm). After NPs incorporation into the chitin matrix, a shift of the absorption edge from UV to the visible region was registered. The bandgap was determined using the Kubelka–Munk remission function defined as $F(R_\infty) = R_\infty(1 - R_\infty)^2/2$, where $R_\infty = R_{sample}/R_{standard}$. The indirect bandgap was obtained by plotting $[\alpha h\nu]^{1/2}$ as a function of the energy [eV] and linearly extrapolating the linear portion $to y = 0$, where α was the absorption coefficient ($F(R_\infty)$) h was Planck's constant, and ν was the frequency of the incident photons (Figure 6b). The pure NPs showed values of 3.03 and 3.14 eV of the indirect bandgap for TiO_2

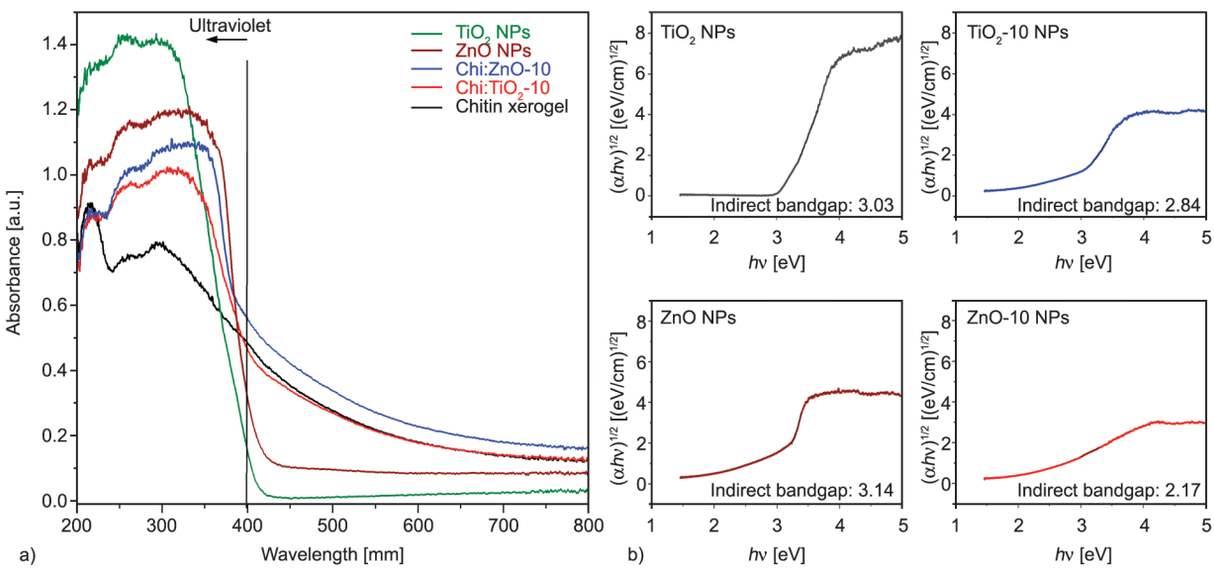

Figure 6. Diffuse reflectance spectra (a) and Kubelka-Munk transform of diffuse reflectance data (b) for the chitin xerogel, TiO_2 NPs, ZnO NPs and their nanocomposites.

and ZnO, respectively. The introduction of TiO_2 and ZnO NPs into the chitin polymeric matrix decreased the indirect bandgap values (2.84 and 2.17, respectively) in both nanocomposite systems. Thus, the bandgap lowering effect was more pronounced for the ZnO-containing material. Also, the absorption for Chi:ZnO-10 was higher than for both components. This change was probably related to NPs stabilization and distribution in the chitin matrix, which implied a higher exposed NP surface for interfacial interaction. These results were in agreement with the reported in the literature for other NPs-polymer systems [45, 46].

3.7. Photocurrent

The photoelectrochemical performances of the NPs and nanocomposites were evaluated by means of photocurrent measurement and thus indirectly determined their capacity of generating and transferring the photo-generated charge carriers. As shown in Figure 7, both NPs and nanocomposites displayed stable trends among light on and off cycles. As it was expected, the photocurrent for the composites was lower than for the nude NPs due to the loading level of the NPs in the chitin matrix. Nevertheless, the chitin matrix showed not to block light transmission to the semiconductors or the electron transport to the electrodes. These would indicate that the nanocomposites would be active for the generation of reactive species that would intermediate in the photocatalytic degradation of organic pollutants.

3.8. Photocatalytic degradation under simulated sunlight irradiation

Dark assays were performed for all cases, and the lack of TMP adsorption capacity by the NPs, chitin, and nanocomposites was evidenced. Thus, the removal of TMP was only a consequence of photocatalytic degradation. An important factor that affects the pollutant photodegradation is the nanoparticle loading amount. Chitin xerogel did not present adsorption for TMP or photocatalytic capacity. This highlighted the fact that the addition of nanoparticles (TiO_2 NPs and ZnO NPs) was relevant. Moreover, the chitin network endowed the nanoparticles with a supporting matrix for their easy recovery from the treated solution, enhancing their applicability.

The influence of the nanoparticle loading amounts on the photocatalytic activity of samples was described in Figure 8a. The increase of TiO_2 NPs and ZnO NPs loading amounts in the polymeric matrix resulted in an increase of trimethoprim degradation in both hybrid systems (C/C_0 was significantly different among NPs loadings, $p < 0.05$). This can be explained on the basis that higher NPs loadings into the composite would generate more active sites that are available to promote trimethoprim photocatalytic degradation. At the TMP and NPs loading levels tested, since the decrease in the remaining TMP fraction was proportional to the increase in the NPs content in the composite, the effect of opacity due to the NPs loading seemed negligible. This could also be indicative of a good dispersion of the NPs within the chitin network. Thus, although EDS mapping showed some zones with higher Ti density, the agglomeration would not be significant enough to interfere with light transmission. For this reason, the Chi:TiO_2-10 and Chi:ZnO-10 composites, with the highest filler content, were chosen as the optimum materials to perform the photocatalytic degradation assays. By comparing the nanocomposites degradation of

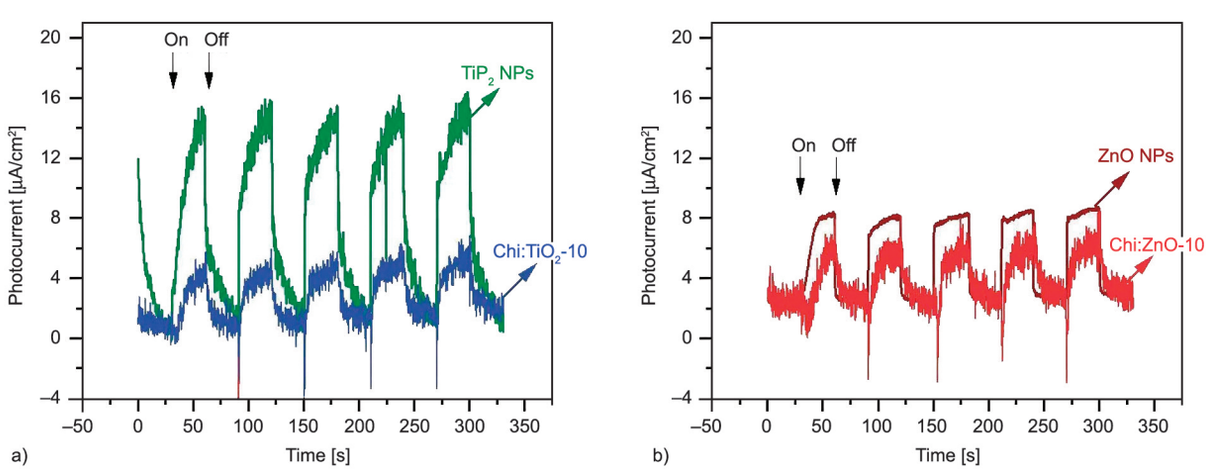

Figure 7. Photocurrent of the TiO_2 NPs, ZnO NPs and nanocomposites under simulated sunlight irradiation. a) TiO_2 NPs and Chi:TiO_2-10, b) ZnO NPs and Chi:ZnO-10.

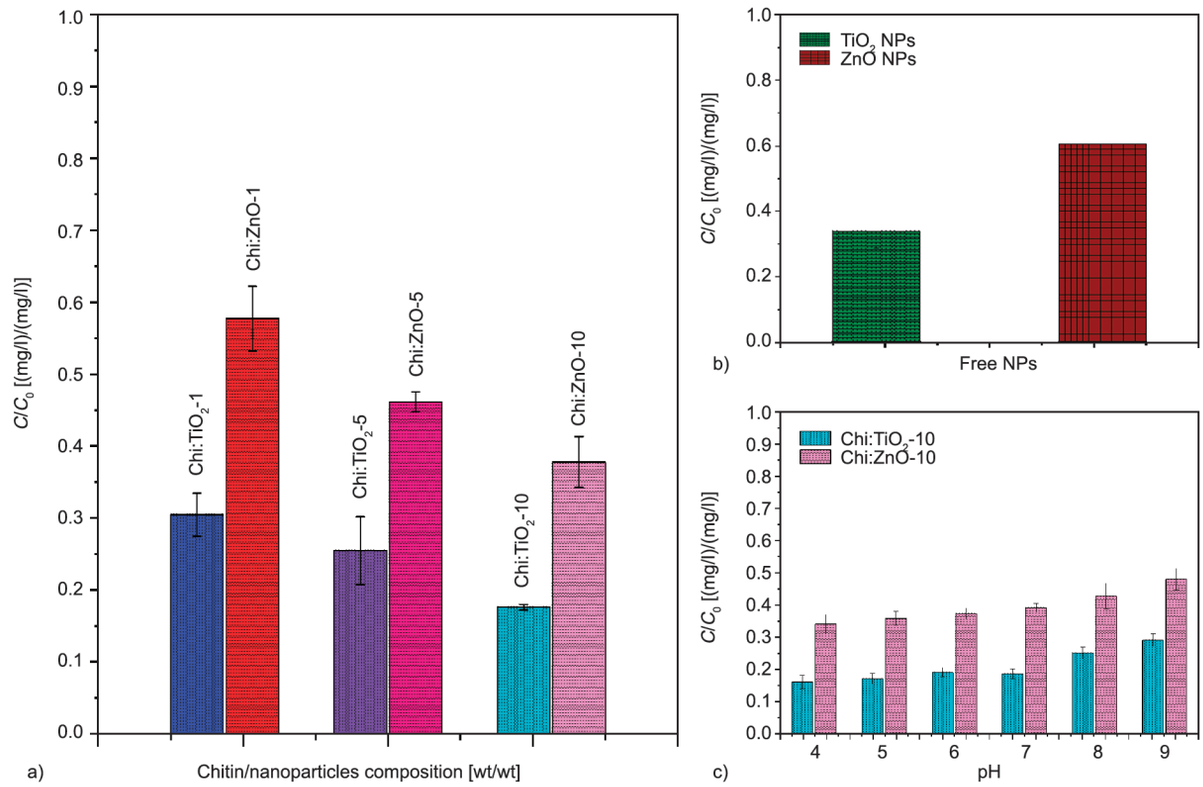

Figure 8. TMP degradation capacity of a) nanocomposites with different chitin:NPs ratio (C_0 = 20 mg·l^{-1}), b) nude NPs (C_0 = 50 mg·l^{-1}), and c) composites at different medium pH (C_0 = 20 mg·l^{-1}).

trimethoprim, it is clear that Chitin:TiO_2 NPs produced a higher fraction removal than Chitin:ZnO NPs under simulated sunlight. Literature reports claim that the comparison in the degradation performance of both types of NPs does not show a trend towards one or another, but it depends on the molecule to be degraded, the irradiation spectrum, and the surrounding media [47–49]. Herein, we also had to consider the influence of the chitin network (Figure 8b). When comparing the photocatalytic activity for the free NPs with the composites, it could be noticed that the activity of the latter was lower than for the formers. Also, the overall photocatalytic performance of the nanocomposites is lower than for other systems reported for antibiotics degradation [50–53]. This was expected since chitin is a non-conducting polymer that would hinder the electron transport from reaching the surface of the composite particle. Since the reactive species photo-generated in the NPs surface had a short lifetime, it would only be active in the pores of the chitin network and would have a low probability of leaving the nanocomposite particle and reaching the solution bulk. Remarkably, the same relative performance was observed when comparing both free NPs and both nanocomposites photocatalytic activity. In either case, the TiO_2 NPs containing systems' activity is higher than the ZnO NPs containing ones. This would mean that the interaction of chitin with the NPs surfaces was similar, as the DRS and photocurrent experimental results suggested. Also, a suggested reaction pathway of the photodegradation of TMP under the simulated sunlight irradiance employing TiO2 NPs, ZnO NPs, and their composites is illustrated in Figure 9.

To analyze whether the photocatalysis degradation was pH-dependent, a solution of trimethoprim was treated with Chi:TiO_2-10 and Chi:ZnO-10 at different pH values (4, 6, and 8) and exposed to simulate sunlight for 7 h. In Figure 8c, it could be seen that for both composites, there is a decreasing tendency in TMP degradation towards alkaline pH. This was expected since the OH radical production is known to decay at alkaline pHs [54]. According to these results, both hybrid composites were chemically stable, and they can be useful at a wide range of pH values.

In order to evaluate the kinetics of photocatalytic degradation of trimethoprim by the selected materials (Chi:TiO_2-10 and Chi:ZnO-10), the experiments were carried out under simulated sunlight in distilled water, as shown in Figure 10a. When comparing the kinetics of the photocatalytic degradation, a significant difference was found between Chi:TiO_2-10 and

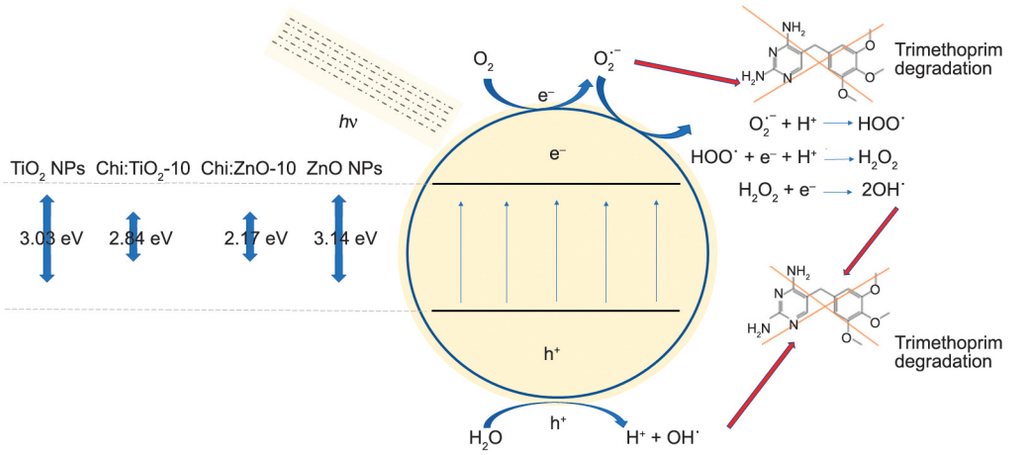

Figure 9. llustrated diagrams of the photodegradation of trimethoprim by ZnO, TiO_2, Chi:TiO_2-and Chi:ZnO-10 nanophotocatalysts.

Chi:ZnO-10. At the conditions used in this research, for the composite based on TiO_2 NPs and chitin, the trimethoprim degradation presented a higher rate, and it was more efficient when compared to Chi:ZnO-10. In both hybrid materials, the degradation rate was higher within the first 4 h. In this time interval, more than 50% of the antibiotic was photocatalytically degraded. After 4 h of light irradiation, the degradation rate rapidly decreased for Chi:TiO_2-10, and the equilibrium was not reached, while for Chi:ZnO-10 the kinetic equilibrium was reached before 4 h.

The degradation kinetics of pollutants by photocatalytic activity depends upon multiple parameters, including organic species deposited, the geometry and porosity of catalyst, light absorption, photocatalyst active species produced, such as $OH^{\cdot}$, $O_2^{\cdot}$, other radicals and h^+ holes [55, 56]. This means that the degradation process does not imply a unique kinetic mechanism, which is decisive in degradation reaction order. The pseudo-first-order and pseudo-second-order models are usually used to describe photocatalytic degradation, especially for antibiotics [57]. Non-linear regression was applied to evaluate the photocatalytic degradation rates using the pseudo-first-order (Equation (5)) and pseudo-second-order (Equation (6)) kinetic equations for trimethoprim degradation, as shown in Figure 10b and 10c, respectively. The fitted parameters are presented in Table 2. According to the analyzed data, photocatalytic degradation of trimethoprim fitted better to a pseudo-second-order kinetic model. A relationship between a better fit of the pseudo-second-order kinetic and the detection of several intermediates due to the generation of sub-products by the photocatalytic degradation oxidation of an organic pollutant was reported previously [58]. The TMP degradation rates observed for the TiO_2-containing composites were twice as higher as for the ZnO-containing ones. This was in accordance with the observed when NPs loadings were compared.

Table 2. The calculated parameters of the pseudo-first-order (Equation (5)) and pseudo-second-order (Equation (6)) model for Chi:TiO_2-10 and Chi:ZnO-10.

Materials	Pseudo-first-order		Pseudo-second-order	
	χ^2	k_1 [h^{-1}]]	χ^2	k_2 [$l \cdot mg^{-1} \cdot h^{-1}$]
Chi:TiO_2-10	2.610	0.28±0.01	0.530	0.0130±0.001
Chi:ZnO-10	9.129	0.13±0.01	5.725	0.0254±0.002

In order to evaluate the reusability and stability of the prepared Chi:TiO_2-10 and Chi:ZnO-10 composites, the TMP degradation process was investigated by reusing the photocatalyst several times. The percentage degradation capacity was calculated by normalizing the degradation fraction of the first use cycle of each experiment as 100%. The results are shown in Figure 10d. As could be observed, the photocatalytic efficiency of both composites was maintained above 95% for at least seven consecutive cycles. ANOVA one-way test did not show a significant difference between photocatalytic efficiencies among cycles for any composite ($p > 0.05$). The degradation efficiency performance obtained in this research was better than the reported in the literature for other nanocomposites. Many of these works do not focus on reusing the photocatalytic system [23]. Others had reported less than 88% degradation efficiency after 4 use cycles using natural polymers without cross-linked support [37, 59]. Also, the present results agreed with the findings of the recent work of Choy *et al.* [25] presented a deeper insight

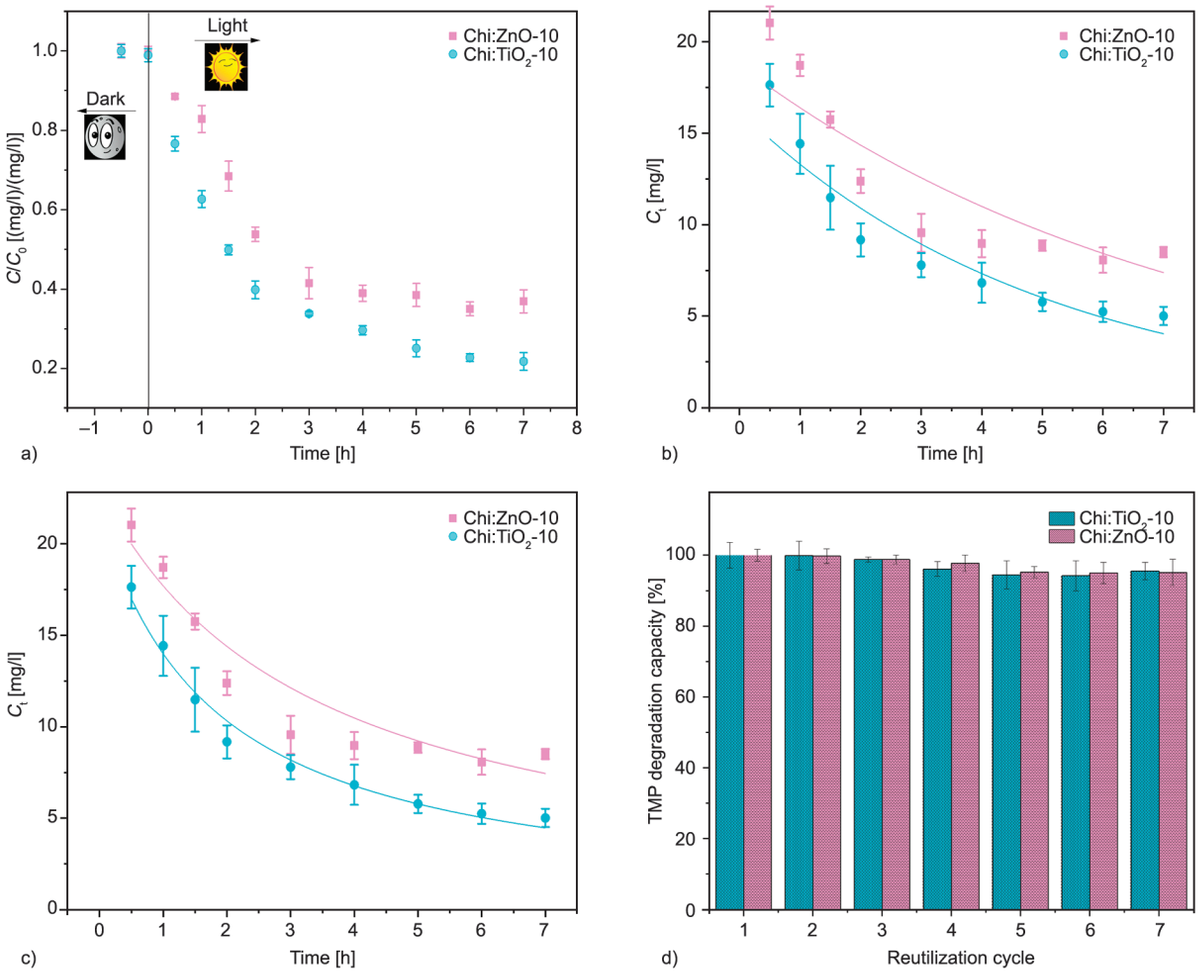

Figure 10. (a) TMP degradation over time (±SD, $n = 3$), (b) fit models are presented: pseudo-first order, (c) pseudo-second-order (respectively) and (d) degradation efficiency of prepared composites on different degradation cycles. Degradation efficiency was normalized using the degradation fraction of the first cycle as 100%.

into the optical properties of these materials and demonstrated the chemical stability of chitin. Furthermore, the weight of the Chi:NPs samples after each consecutive photoreaction was totally recovered. This indicated the good stability of the support and that the prepared composites were easy to handle after subsequent reuses compared with nude NPs. FTIR analyses of the pre-use and post-utilized Chi:TiO_2-10 and Chi:ZnO-10 composites revealed no significant changes compared to the spectrum of the composite without use (Figure 11). The subtle change observed on both composites was related to the band's splitting corresponding to the vibrational stretching of C=O (amide I) (at 1669 cm^{-1}) involved in inter-chain and intra-chain hydrogen bonding. This change would be related to conformational changes due to swelling and drying cycles. This conformational change has also been reported in the literature after chitin dissolution and subsequent crystallization [60]. FTIR spectra from utilized composites

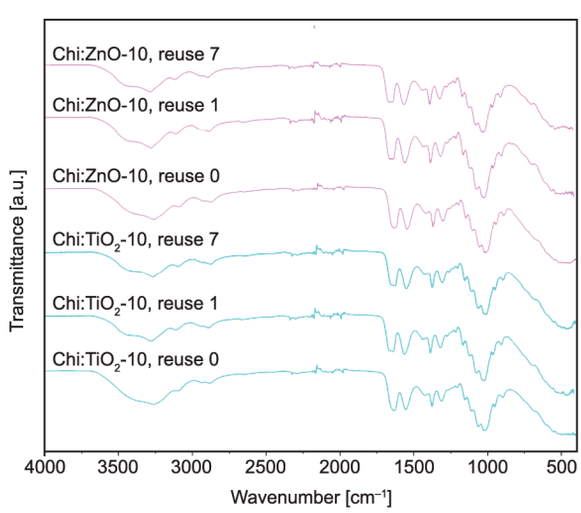

Figure 11. FTIR spectra of Chi:TiO_2-10 and Chi:ZnO-10 after and before the photocatalytic experiments.

did not evidence any significant change in the chitin polymeric matrix structure. From these results, it could be confirmed that the chemical stability of

chitin allowed the nanocomposite to be reused without any photocatalytic damage.

4. Conclusions

Both nanocomposites have demonstrated the potential application for the effective degradation of trimethoprim. The effectiveness of photocatalytic degradation of trimethoprim by Chi:TiO_2-10 composite was better than Chi:ZnO-10 composite under the same experimental conditions. The alkaline medium produced a decrease in the degradation efficiency, but both hybrid composites can be used over a wide range of pH with low variation of their photocatalytic capacity. The experimental data of both hybrid systems showed the best fit to the pseudo-second-order model, and they are good candidates to be used for photocatalytic degradation in addressing the global environmental concern for antibiotics.

Remarkably, chitin chemical structure was not affected by the photocatalytic process, even after several cycles; and the optical properties of the nanoparticles were influenced by their immobilization in chitin by lowering their bandgap and enhancing its photocatalytic efficiency towards the visible-light spectrum.

The use of the chitin opened up the possibility of employing a supported NPs photocatalytic system, promoting visible-light absorption, and also offered an easy way to recover a chemically stable photocatalytic system.

These results suggest that future developments focused on the sustainability of materials and the photocatalytic process should consider the interaction between components for the design of efficient composites.

Acknowledgements

J.J.P.B. is grateful for his postdoctoral fellowship granted by Consejo Nacional de Investigaciones Científicas y Técnicas (CONICET). SEGEMAR for their assistance in XRD measurements. The authors would like to acknowledge INTI Mecánica and M. Pianetti for their assistance in SEM analysis. This work was supported with grants from Universidad de Buenos Aires (UBACyT 20020170100125BA, UBACyT 20020190100265BA) and Agencia Nacional de Promoción Científica y Tecnológica (PICT 2018-01731, PICT 2019-03757).

References

[1] Geissen V., Mol H., Klumpp E., Umlauf G., Nadal M., van der Ploeg M., van de Zee S. E. A. T. M., Ritsema C. J.: Emerging pollutants in the environment: A challenge for water resource management. International Soil and Water Conservation Research, **3**, 57–65 (2015). https://doi.org/10.1016/j.iswcr.2015.03.002

[2] Teodosiu C., Gilca A-F., Barjoveanu G., Fiore S.: Emerging pollutants removal through advanced drinking water treatment: A review on processes and environmental performances assessment. Journal of Cleaner Production, **197**, 1210–1221 (2018). https://doi.org/10.1016/j.jclepro.2018.06.247

[3] Cai Q., Hu J.: Effect of UVA/LED/TiO_2 photocatalysis treated sulfamethoxazole and trimethoprim containing wastewater on antibiotic resistance development in sequencing batch reactors. Water Research, **140**, 251–260 (2018). https://doi.org/10.1016/j.watres.2018.04.053

[4] Perez J. J., Villanueva M. E., Sánchez L., Ollier R., Alvarez V., Copello G. J.: Low cost and regenerable composites based on chitin/bentonite for the adsorption potential emerging pollutants. Applied Clay Science, **194**, 105703 (2020). https://doi.org/10.1016/j.clay.2020.105703

[5] Sousa J. C. G., Ribeiro A. R., Barbosa M. O., Pereira M. F. R., Silva A. M. T.: A review on environmental monitoring of water organic pollutants identified by EU guidelines. Journal of Hazardous Materials, **344**, 146–162 (2018). https://doi.org/10.1016/j.jhazmat.2017.09.058

[6] Deblonde T., Cossu-Leguille C., Hartemann P.: Emerging pollutants in wastewater: A review of the literature. International Journal of Hygiene and Environmental Health, **214**, 442–448 (2011). https://doi.org/10.1016/j.ijheh.2011.08.002

[7] Martínez-Costa J. I., Maldonado Rubio M. I., Leyva-Ramos R.: Degradation of emerging contaminants diclofenac, sulfamethoxazole, trimethoprim and carbamazepine by bentonite and vermiculite at a pilot solar compound parabolic collector. Catalysis Today, **341**, 26–36 (2020). https://doi.org/10.1016/j.cattod.2018.07.021

[8] Khakpash N., Simchi A., Jafari T.: Adsorption and solar light activity of transition-metal doped TiO_2 nanoparticles as semiconductor photocatalyst. Journal of Materials Science: Materials in Electronics, **23**, 659–667 (2012). https://doi.org/10.1007/s10854-011-0466-y

[9] Tobajas M., Belver C., Rodriguez J. J.: Degradation of emerging pollutants in water under solar irradiation using novel TiO_2-ZnO/clay nanoarchitectures. Chemical Engineering Journal, **309**, 596–606 (2017). https://doi.org/10.1016/j.cej.2016.10.002

[10] Banan A., Bayat A., Valizadeh H.: Copper immobilized onto polymer-coated magnetic nanoparticles as recoverable catalyst for 'click' reaction. Applied Organometallic Chemistry, **31**, e3604 (2017). https://doi.org/10.1002/aoc.3604

[11] Sharma G., Kumar A., Naushad M., Thakur B., Vo D-V. N., Gao B., Al-Kahtani A. A., Stadler F. J.: Adsorptional-photocatalytic removal of fast sulphon black dye by using chitin-cl-poly(itaconic acid-co-acrylamide)/zirconium tungstate nanocomposite hydrogel. Journal of Hazardous Materials, **416**, 125714 (2021). https://doi.org/10.1016/j.jhazmat.2021.125714

[12] Sukumaran N. P., Gopi S.: Overview of biopolymers: resources, demands, sustainability, and life cycle assessment modeling and simulation. in 'Biopolymers and their industrial applications' (eds.: Thomas S., Gopi S., Amalraj A.) Elsevier, Amsterdam, 1–19 (2021). https://doi.org/10.1016/B978-0-12-819240-5.00001-8

[13] Peralta Ramos M. L., González J. A., Albornoz S. G., Pérez C. J., Villanueva M. E., Giorgieri S. A., Copello G. J.: Chitin hydrogel reinforced with TiO_2 nanoparticles as an arsenic sorbent. Chemical Engineering Journal, **285**, 581–587 (2016). https://doi.org/10.1016/j.cej.2015.10.035

[14] Sun C., Wang Z., Chen L., Li F.: Fabrication of robust and compressive chitin and graphene oxide sponges for removal of microplastics with different functional groups. Chemical Engineering Journal, **393**, 124796 (2020). https://doi.org/10.1016/j.cej.2020.124796

[15] Roy J. C., Salaün F., Giraud S., Ferri A.: Solubility of chitin: Solvents, solution behaviors and their related mechanisms. in 'Solubility of polysaccharides' (ed.: Xu Z.) InTech, London, 109-128 (2017). https://doi.org/10.5772/intechopen.71385

[16] Fang Y., Duan B., Lu A., Liu M., Liu H., Xu X., Zhang L.: Intermolecular interaction and the extended worm-like chain conformation of chitin in NaOH/urea aqueous solution. Biomacromolecules, **16**, 1410–1417 (2015). https://doi.org/10.1021/acs.biomac.5b00195

[17] González J. A., Bafico J. G., Villanueva M. E., Giorgieri S. A., Copello G. J.: Continuous flow adsorption of ciprofloxacin by using a nanostructured chitin/graphene oxide hybrid material. Carbohydrate Polymers, **188**, 213–220 (2018). https://doi.org/10.1016/j.carbpol.2018.02.021

[18] Pei X., Li Y., Deng Y., Lu L., Li W., Shi R., Lei A., Zhang L.: Chitin microsphere supported Pd nanoparticles as an efficient and recoverable catalyst for CO oxidation and Heck coupling reaction. Carbohydrate Polymers, **251**, 117020 (2021). https://doi.org/10.1016/j.carbpol.2020.117020

[19] Zhang Z., Katba Bader Y. M., Yang J., Lucia L. A.: Simultaneously improved chitin gel formation and thermal stability promoted by TiO_2. Journal of Molecular Liquids, **328**, 115332 (2021). https://doi.org/10.1016/j.molliq.2021.115332

[20] Duan B., Liu F., He M., Zhang L.: Ag–Fe_3O_4 nanocomposites@chitin microspheres constructed by *in situ* one-pot synthesis for rapid hydrogenation catalysis. Green Chemistry, **16**, 2835–2845 (2014). https://doi.org/10.1039/C3GC42637H

[21] Zhu K., Shi S., Cao Y., Lu A., Hu J., Zhang L.: Robust chitin films with good biocompatibility and breathable properties. Carbohydrate Polymers, **212**, 361–367 (2019). https://doi.org/10.1016/j.carbpol.2019.02.054

[22] Lin X., Yang A., Huang G., Zhou X., Zhai Y., Chen X., McBean E.: Treatment of aquaculture wastewater through chitin/ZnO composite photocatalyst. Water, **11**, 310 (2019). https://doi.org/10.3390/w11020310

[23] Sadjadi S., Koohestani F., Mahmoodi N. M., Rabeie B.: Composite of MOF and chitin as an efficient catalyst for photodegradation of organic dyes. International Journal of Biological Macromolecules, **182**, 524–533 (2021). https://doi.org/10.1016/j.ijbiomac.2021.04.034

[24] Wang Y., Li Y., Liu S., Li B.: Fabrication of chitin microspheres and their multipurpose application as catalyst support and adsorbent. Carbohydrate Polymers, **120**, 53–59 (2015). https://doi.org/10.1016/j.carbpol.2014.12.005

[25] Choy S., Bui H. T., Lam D. V., Lee S-M., Kim W., Hwang D. S.: Photocatalytic exoskeleton: Chitin nanofiber for retrievable and sustainable TiO_2 carriers for the decomposition of various pollutants. Carbohydrate Polymers, **271**, 118413 (2021). https://doi.org/10.1016/j.carbpol.2021.118413

[26] Villanueva M. E., Cuestas M. L., Pérez C. J., Dall' Orto V. C., Copello G. J.: Smart release of antimicrobial ZnO nanoplates from a pH-responsive keratin hydrogel. Journal of Colloid and Interface Science, **536**, 372–380 (2019). https://doi.org/10.1016/j.jcis.2018.10.067

[27] Meulenkamp E. A.: Synthesis and growth of ZnO nanoparticles. The Journal of Physical Chemistry B, **102**, 5566–5572 (1998). https://doi.org/10.1021/jp980730h

[28] Brugnerotto J., Lizardi J., Goycoolea F. M., Argüelles-Monal W., Desbrières J., Rinaudo M.: An infrared investigation in relation with chitin and chitosan characterization. Polymer, **42**, 3569–3580 (2001). https://doi.org/10.1016/S0032-3861(00)00713-8

[29] Segal L., Creely J. J., Martin A. E., Conrad C. M.: An empirical method for estimating the degree of crystallinity of native cellulose using the X-ray diffractometer. Textile Research Journal, **29**, 786–794 (1959). https://doi.org/10.1177/004051755902901003

[30] Tan T. S., Chin H. Y., Tsai M-L., Liu C-L.: Structural alterations, pore generation, and deacetylation of α- and β-chitin submitted to steam explosion. Carbohydrate Polymers, **122**, 321–328 (2015). https://doi.org/10.1016/j.carbpol.2015.01.016

[31] Bhardwaj R., Bharti A., Singh J. P., Chae K. H., Goyal N., Gautam S.: Structural and electronic investigation of ZnO nanostructures synthesized under different environments. Heliyon, **4**, e00594 (2018). https://doi.org/10.1016/j.heliyon.2018.e00594

[32] Ward M. D., Bard A. J.: Photocurrent enhancement *via* trapping of photogenerated electrons of titanium dioxide particles. The Journal of Physical Chemistry, **86**, 3599–3605 (1982). https://doi.org/10.1021/j100215a021

[33] Nisar A., Saeed M., Usman M., Muneer M., Adeel M., Khan I., Akhtar J.: Kinetic modeling of ZnO-rGO catalyzed degradation of methylene blue. International Journal of Chemical Kinetics, **52**, 645–654 (2020). https://doi.org/10.1002/kin.21389

[34] El Knidri H., Belaabed R., Addaou A., Laajeb A., Lahsini A.: Extraction, chemical modification and characterization of chitin and chitosan. International Journal of Biological Macromolecules, **120**, 1181–1189 (2018). https://doi.org/10.1016/j.ijbiomac.2018.08.139

[35] Kim S-H., Ngo H. H., Shon H. K., Vigneswaran S.: Adsorption and photocatalysis kinetics of herbicide onto titanium oxide and powdered activated carbon. Separation and Purification Technology, **58**, 335–342 (2008). https://doi.org/10.1016/j.seppur.2007.05.035

[36] Jang M-K., Kong B-G., Jeong Y-I., Lee C. H., Nah J-W.: Physicochemical characterization of α-chitin, β-chitin, and γ-chitin separated from natural resources. Journal of Polymer Science Part A: Polymer Chemistry, **42**, 3423–3432 (2004). https://doi.org/10.1002/pola.20176

[37] Villanueva M. E., Puca M., Pérez Bravo J., Bafico J., Dall Orto V. C., Copello G. J.: Dual adsorbent-photocatalytic keratin–TiO_2 nanocomposite for trimethoprim removal from wastewater. New Journal of Chemistry, **44**, 10964–10972 (2020). https://doi.org/10.1039/D0NJ02784G

[38] Oun A. A., Rhim J-W.: Preparation of multifunctional chitin nanowhiskers/ZnO-Ag NPs and their effect on the properties of carboxymethyl cellulose-based nanocomposite film. Carbohydrate Polymers, **169**, 467–479 (2017). https://doi.org/10.1016/j.carbpol.2017.04.042

[39] Kakiuchi K., Hosono E., Kimura T., Imai H., Fujihara S.: Fabrication of mesoporous ZnO nanosheets from precursor templates grown in aqueous solutions. Journal of Sol-Gel Science and Technology, **39**, 63–72 (2006). https://doi.org/10.1007/s10971-006-6321-6

[40] Song H., Yang H., Ma X.: A comparative study of porous ZnO nanostructures synthesized from different zinc salts as gas sensor materials. Journal of Alloys and Compounds, **578**, 272–278 (2013). https://doi.org/10.1016/j.jallcom.2013.05.211

[41] Sun D., Wong M., Sun L., Li Y., Miyatake N., Sue H-J.: Purification and stabilization of colloidal ZnO nanoparticles in methanol. Journal of Sol-Gel Science and Technology, **43**, 237–243 (2007). https://doi.org/10.1007/s10971-007-1569-z

[42] Takegawa A., Murakami M., Kaneko Y., Kadokawa J.: Preparation of chitin/cellulose composite gels and films with ionic liquids. Carbohydrate Polymers, **79**, 85–90 (2010). https://doi.org/10.1016/j.carbpol.2009.07.030

[43] Shankar S., Teng X., Li G., Rhim J-W.: Preparation, characterization, and antimicrobial activity of gelatin/ZnO nanocomposite films. Food Hydrocolloids, **45**, 264–271 (2015). https://doi.org/10.1016/j.foodhyd.2014.12.001

[44] Nosal W. H., Thompson D. W., Yan L., Sarkar S., Subramanian A., Woollam J. A.: UV–vis–infrared optical and AFM study of spin-cast chitosan films. Colloids and Surfaces B: Biointerfaces, **43**, 131–137 (2005). https://doi.org/10.1016/j.colsurfb.2004.08.022

[45] Flores-Moreno A., Herrera-González A. M., García-Serrano J.: Modification of the crystal lattice and optical band gap of ZnO nanostructures by the polyelectrolytes presence. Journal of Materials Science: Materials in Electronics, **29**, 15604–15612 (2018). https://doi.org/10.1007/s10854-018-9152-7

[46] Praveena S. D., Ravindrachary V., Bhajantri R. F., Ismayil: Dopant-induced microstructural, optical, and electrical properties of TiO_2/PVA composite. Polymer Composites, **37**, 987–997 (2016). https://doi.org/10.1002/pc.23258

[47] Han J., Liu Y., Singhal N., Wang L., Gao W.: Comparative photocatalytic degradation of estrone in water by ZnO and TiO_2 under artificial UVA and solar irradiation. Chemical Engineering Journal, **213**, 150–162 (2012). https://doi.org/10.1016/j.cej.2012.09.066

[48] Sakthivel S., Neppolian B., Shankar M. V., Arabindoo B., Palanichamy M., Murugesan V.: Solar photocatalytic degradation of azo dye: Comparison of photocatalytic efficiency of ZnO and TiO_2. Solar Energy Materials and Solar Cells, **77**, 65–82 (2003). https://doi.org/10.1016/S0927-0248(02)00255-6

[49] Štrbac D., Aggelopoulos C. A., Štrbac G., Dimitropoulos M., Novaković M., Ivetić T., Yannopoulos S. N.: Photocatalytic degradation of naproxen and methylene blue: Comparison between ZnO, TiO_2 and their mixture. Process Safety and Environmental Protection, **113**, 174–183 (2018). https://doi.org/10.1016/j.psep.2017.10.007

[50] Kumar A., Thakur P. R., Sharma G., Vo D-V. N., Naushad M., Tatarchuk T., García-Peñas A., Du B., Stadler F. J.: Accelerated charge transfer in well-designed S-scheme Fe@TiO_2/boron carbon nitride heterostructures for high performance tetracycline removal and selective photo-reduction of CO_2 greenhouse gas into CH_4 fuel. Chemosphere, **287**, 132301 (2022). https://doi.org/10.1016/j.chemosphere.2021.132301

[51] Kumar A., Sharma G., Kumari A., Guo C., Naushad M., Vo D-V. N., Iqbal J., Stadler F. J.: Construction of dual Z-scheme g-C_3N_4/$Bi_4Ti_3O_{12}$/$Bi_4O_5I_2$ heterojunction for visible and solar powered coupled photocatalytic antibiotic degradation and hydrogen production: Boosting *via* I^-/I_3^- and Bi^{3+}/Bi^{5+} redox mediators. Applied Catalysis B: Environmental, **284**, 119808 (2021). https://doi.org/10.1016/j.apcatb.2020.119808

[52] Sharma G., Bhogal S., Kumar A., Naushad M., Sharma S., Ahamad T., Stadler F. J.: AgO/MgO/FeO@Si_3N_4 nanocomposite with robust adsorption capacity for tetracycline antibiotic removal from aqueous system. Advanced Powder Technology, **31**, 4310–4318 (2020). https://doi.org/10.1016/j.apt.2020.09.006

[53] Sharma S. K., Kumar A., Sharma G., Stadler F. J., Naushad M., Ghfar A. A., Ahamad T.: LaTiO*2*N/Bi*2*S*3* Z-scheme nano heterostructures modified by rGO with high interfacial contact for rapid photocatalytic degradation of tetracycline. Journal of Molecular Liquids, **311**, 113300 (2020). https://doi.org/10.1016/j.molliq.2020.113300

[54] Nakabayashi Y., Nosaka Y.: The pH dependence of OH radical formation in photo-electrochemical water oxidation with rutile TiO_2 single crystals. Physical Chemistry Chemical Physics, **17**, 30570–30576 (2015). https://doi.org/10.1039/C5CP04531B

[55] Friedmann D., Mendive C., Bahnemann D.: TiO_2 for water treatment: Parameters affecting the kinetics and mechanisms of photocatalysis. Applied Catalysis B: Environmental, **99**, 398–406 (2010). https://doi.org/10.1016/j.apcatb.2010.05.014

[56] Turchi C., Ollis D. F.: Photocatalytic degradation of organic water contaminants: Mechanisms involving hydroxyl radical attack. Journal of Catalysis, **122**, 178–192 (1990). https://doi.org/10.1016/0021-9517(90)90269-P

[57] Kazeminezhad I., Sadollahkhani A.: Influence of pH on the photocatalytic activity of ZnO nanoparticles. Journal of Materials Science: Materials in Electronics, **27**, 4206–4215 (2016). https://doi.org/10.1007/s10854-016-4284-0

[58] Zhou S., Du Z., Li X., Zhang Y., He Y., Zhang Y.: Degradation of methylene blue by natural manganese oxides: Kinetics and transformation products. Royal Society Open Science, **6**, 190351 (2019). https://doi.org/10.1098/rsos.190351

[59] Zhao Y., Tao C., Xiao G., Su H.: Controlled synthesis and wastewater treatment of Ag_2O/TiO_2 modified chitosan-based photocatalytic film. RSC Advances, **7**, 11211–11221 (2017). https://doi.org/10.1039/C6RA27295A

[60] Chang C., Chen S., Zhang L.: Novel hydrogels prepared via direct dissolution of chitin at low temperature: Structure and biocompatibility. Journal of Materials Chemistry, **21**, 3865 (2011). https://doi.org/10.1039/c0jm03075a